

## Lateral force calibration of an atomic force microscope with a diamagnetic levitation spring system

Q. Li, K.-S. Kim, and A. Rydberg

*Division of Engineering, Brown University, Providence, Rhode Island 02912*

(Received 4 December 2005; accepted 24 April 2006; published online 14 June 2006)

A novel diamagnetic lateral force calibrator (D-LFC) has been developed to directly calibrate atomic force microscope (AFM) cantilever-tip or -bead assemblies. This enables an AFM to accurately measure the lateral forces encountered in friction or biomechanical-testing experiments at a small length scale. In the process of development, deformation characteristics of the AFM cantilever assemblies under frictional loading have been analyzed and four essential response variables, i.e., force constants, of the assembly have been identified. Calibration of the lateral force constant and the “crosstalk” lateral force constant, among the four, provides the capability of measuring absolute AFM lateral forces. The D-LFC is composed of four NdFeB magnets and a diamagnetic pyrolytic graphite sheet, which can calibrate the two constants with an accuracy on the order of 0.1%. Preparation of the D-LFC and the data processing required to get the force constants is significantly simpler than any other calibration methods. The most up-to-date calibration technique, known as the “wedge method,” calibrates mainly one of the two constants and, if the crosstalk effect is properly analyzed, is primarily applicable to a sharp tip. In contrast, the D-LFC can calibrate both constants simultaneously for AFM tips or beads with any radius of curvature. These capabilities can extend the applicability of AFM lateral force measurement to studies of anisotropic multiscale friction processes and biomechanical behavior of cells and molecules under combined loading. Details of the D-LFC method as well as a comparison with the wedge method are provided in this article. © 2006 American Institute of Physics. [DOI: [10.1063/1.2209953](https://doi.org/10.1063/1.2209953)]

### I. INTRODUCTION

From its inception,<sup>1</sup> atomic force microscopes (AFM) have been widely used for studying nanoscale friction properties.<sup>2–4</sup> The most commonly used experimental apparatus for AFM friction measurements consists of a cantilever-tip assembly and its force transducers. The tip is typically made of a silicon or silicon nitride apex formed by chemical etching, or a bead of a few micrometers in radius, sometimes called a colloid tip,<sup>5,6</sup> attached to a thin silicon or silicon nitride film cantilever. The transducer is commonly made of a position sensitive photodetector (PSPD) array, which senses the deflection of a laser beam reflected off the top surface of the AFM cantilever near the end. The deflection of the laser beam is generated by the bending and torsional deformations of the cantilever, which are caused by normal contact and friction forces exerted by the substrate material surface against the tip.

However, for as long as AFM has been used to study the frictional properties of materials at the nanoscale, there have been difficulties in measuring the absolute lateral force components involved in the friction process. The friction force detected as a lateral force on the AFM cantilever induces the torsional deformation, i.e., twist, of the cantilever; however, the normal force also contributes to the twist. The effect of the normal force on the twist of the cantilever is known as the “crosstalk” effect.<sup>4</sup> Generally speaking, the crosstalk can be induced mechanically, i.e., the *shear center* misalignment of the cantilever with respect to the geometric center of the

cantilever, and optically, i.e., the misalignment of the PSPD array. The conventional method of avoiding the crosstalk effect was to hold the normal force constant during a friction test and measure the relative friction force between the forward and backward sliding processes. However, this method cannot measure the absolute frictional lateral force if the absolute values of the frictional forces for forward and backward sliding processes are different from each other. In addition, the most current technique, the “wedge” method employed in the wedge lateral force calibrator (W-LFC),<sup>4,7</sup> is only valid for a sharp AFM tip, with a negligible radius of curvature compared to the tip height, if the crosstalk caused by misalignment of the shear center is properly taken into account. However, it is required to use a tip of a relatively large radius of curvature for studying scale effects of friction and biomechanical testing of cells and molecules. For such a large radius of curvature, a bead is usually attached to the AFM cantilever, and the system of equations to convert the AFM signals of the wedge calibration to the lateral force constant has too many variables to have a unique solution, if the mechanical crosstalk effect is considered properly. Therefore, there has been great demand to develop a robust method of accurately measuring the absolute lateral forces exerted on the AFM bead with a relatively large radius of curvature.

In this article we present a new apparatus, the diamagnetic lateral force calibrator (D-LFC), which provides a direct means of calibrating an AFM to measure the absolute lateral forces exerted on the AFM tip or bead. In order to

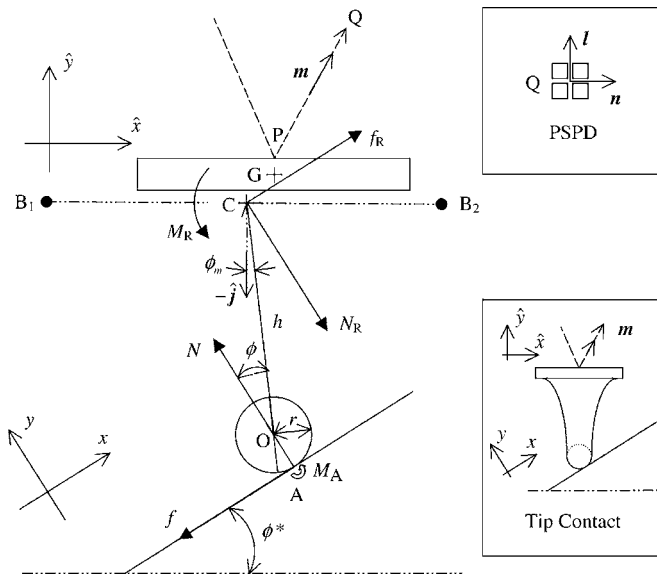


FIG. 1. Free body diagram of an AFM cantilever-tip assembly on a projection plane showing a deformed configuration:  $N$  is the normal force,  $f$  the friction force,  $M_A$  the adhesion moment, and subscript  $R$  indicates reaction forces and moment;  $G$ ,  $C$ , and  $O$  denote the geometrical center, shear center of the cantilever, and the center of the tip curvature, respectively;  $B_1$ – $B_2$  represents the principal axis of bending,  $\phi_m$  the tip misfit angle, and  $\phi^*$  the substrate slope angle; dashed line depicts the laser light path;  $(x, y)$  are the force coordinates,  $(\hat{x}, \hat{y})$  the cantilever coordinates, and  $(l, n)$  shown in the upper inset are the PSPD sensing directions. The lower inset shows the outline of the tip for the free body diagram.

make a comprehensive presentation and to make objective comparisons with other calibration methods, we introduce an analysis of the AFM friction test system in the following section.

### A. Deformation and transducer characteristics of an AFM friction test system

Figure 1 shows a free body diagram of an AFM cantilever-tip assembly on a projection plane, showing a front end view of the deformed configuration. However, since it is a small twist configuration, the cross section of the cantilever is not rotated pictorially in the figure and the small angle of twist  $\Delta\phi$  caused by the deformation is imbedded in  $\phi$ . The projection plane is the one which passes through the geometrical contact point  $A$  and is parallel to the plane defined by the vectors  $l$  and  $m$  shown in the figure. The vector  $m$  is a unit vector in the direction from the point  $P$  of laser reflection on the AFM cantilever to the center point  $Q$  of the PSPD. We have drawn a laser illumination configuration that our AFM (PSI AutoCP) employed. However, the orientation of laser illumination can be in any direction, in general. The lateral force sensing vector  $l$  is a unit vector on the plane of the PSPD in the direction of sensing the laser beam deflection caused by torsional twist of the AFM cantilever. The other normal force sensing vector  $n$ , shown in the upper inset of Fig. 1, is the direction of sensing the laser beam deflection induced by bending the cantilever. In this section we will only consider the mechanical crosstalk effect, and the optical misalignment effect will be discussed separately in a later section.

The point  $O$  is the center of curvature of the tip and the point  $C$  is the shear center of the AFM cantilever. The shear center is a spatial point of structural significance at which any resultant concentrated force cannot induce a torsional twist on the cantilever. The location of the shear center on the projection plane is unique and depends on the distribution of the elastic moduli and the global geometry of the cantilever structure. In general, the shear center  $C$  is distinctly displaced from the geometrical center  $G$  of the local cross section of the cantilever on the projection plane. For example, we estimated the location of the shear center based on direct optical imaging of the planar geometry and the tip location of a noncontact C-type triangular cantilever, using the ABAQUS finite element analysis. The finite element method (FEM) analysis shows that the misalignment of the shear center was approximately  $3 \mu\text{m}$  in a lateral direction. The tip had a height of  $4 \mu\text{m}$ . The misalignment could have been much worse, if we had the asymmetry of the tip location like the one shown in Fig. 2 of Ref. 4. The local cross section of the cantilever is depicted by a rectangle in Fig. 1. It is assumed that the AFM tip is locally spherical, with a radius  $r$  near the contact point. The tip is represented by a circle in the figure. Also, it is assumed that the nominal surface normal of the undeformed substrate at the contact point is aligned with the line  $AO$ , which lies on the projection plane. The distance between the points  $O$  and  $C$  is denoted by  $h$ , while the angle between  $AO$  and  $OC$  is depicted by  $\phi$ . The angle  $\phi = \phi_0 + \Delta\phi$  is composed of the initial tilt angle  $\phi_0$  in the undeformed configuration and the angle of twist  $\Delta\phi$  caused by the deformation.

The diagrams of Fig. 1 are illustrated in three major activity coordinates. One is the friction force coordinates  $(x, y)$ , another the mechanical sensing coordinates  $(\hat{x}, \hat{y})$ , and the last, the optical sensing coordinate directions  $(n, l)$ . The  $x$  coordinate is aligned with the intersection between the projection plane and the tip-contact surface of the substrate, and the  $y$  coordinate with the normal of the surface as shown in the figure. The mechanical sensing coordinate,  $\hat{x}$ , is lined up with the principal axis ( $B_1$ – $B_2$ ) of the bending stiffness of the thin film cantilever, which is assumed to be parallel to the top surface of the cantilever at the laser reflection point  $P$ . The  $\hat{y}$  coordinate is in the normal direction to the top surface. We will describe the forces of the contact friction in the  $(x, y)$  coordinates and the deformation of the cantilever in the  $(\hat{x}, \hat{y})$  coordinates, and then derive the relationship between the forces and the deformation quantities.

The force balance in the  $x$  and  $y$  directions requires  $f_R = f$  and  $N_R = N$ , where  $f$  denotes the lateral force and  $N$  the normal force at the contact point, while the subscript  $R$  indicates the reaction forces at the root of the AFM cantilever. The moment balance with respect to the shear center  $C$  is simply reduced to

$$M_R = Nh \sin \phi + f(h \cos \phi + r) - M_A, \quad (1)$$

where  $M_A$  stands for the contact moment induced by the asymmetry of the adhesive contact stress distribution. Then, the torsional reaction moment  $M_R$  is related to the elastic torsional deformation  $\Delta\phi$  of the AFM cantilever as

$$M_R = \kappa \Delta\phi, \quad (2)$$

where  $\kappa$  is the *torsional spring constant* of the cantilever. As we operate the AFM in a small deformation range of  $\Delta\phi \ll 1$ , Eqs. (1) and (2) can be further reduced to a fundamental equation of twist as

$$Nh \sin \phi_0 + f(h \cos \phi_0 + r) - M_A = \kappa^* \Delta\phi, \quad (3)$$

where the effective torsional spring constant  $\kappa^* = (\kappa - Nh \cos \phi_0 + fh \sin \phi_0)$  reduces to  $\kappa^* \cong \kappa$  for  $Nh/\kappa \ll 1$  and  $fh/\kappa \ll 1$ . The maximum value of  $Nh/\kappa$  and  $fh/\kappa$  is less than  $10^{-3}$  for typical AFM friction tests.

In the AFM friction test the output voltage  $\hat{V}^{(l)}$  of the lateral direction PSPD, with respect to the twist angle  $\Delta\phi$ , can be represented by

$$\hat{V}^{(l)} = \beta_l \Delta\phi, \quad (4)$$

where  $\beta_l$  is the lateral *angle sensitivity constant* of the PSPD, in V/rad. It is noticed that our definition of  $\beta_l$  gives the relationship  $\beta_l = \kappa/\beta$ , with the calibration constant  $\beta$  used by Varenberg *et al.*<sup>7</sup> Denoting the substrate angle between  $x$  and  $\hat{x}$  as  $\phi^*$ , and the shear center misfit angle between  $OC$  and  $\hat{y}$  as  $\phi_m$ , we have the relationship  $\phi_0 = \phi^* - \phi_m$ , and (3) can be expanded to

$$N_\eta(1 - \xi)\sin(\phi^* - \phi_m) + \text{sgn}(\eta)f_\eta\{(1 - \xi)\cos(\phi^* - \phi_m) + \xi\} = \alpha_l \hat{V}_\eta^{(l)}, \quad \text{for } \eta = a \text{ or } b, \quad (5)$$

where  $\xi = r/H$ , with  $H = h + r$ , and  $\text{sgn}(\eta) = 1$  for  $\eta = a$  and  $-1$  for  $\eta = b$ , with  $a$  and  $b$  denoting the quantities associated with frictional loading in the forward ( $+\hat{x}$ ) and backward ( $-\hat{x}$ ) directions, respectively. Here, it is assumed that  $M_A/(f_\eta H) \ll 1$ , where  $M_A$  is a function of  $f$  and  $N$ , in general. The *generic lateral force constant*  $\alpha_l$  of the AFM friction measurement appearing on the right hand side of (5) is defined by

$$\alpha_l = \kappa/(\beta_l H). \quad (6)$$

The generic lateral force constant  $\alpha_l$  can be directly calibrated if the substrate angle is adjusted to be  $\phi_0 = \phi^* - \phi_m = 0$  by regulating the variation of the lateral PSPD output,  $\hat{V}^{(l)}$ , to vanish when the normal load  $N$  is altered. Then, the relationship between the lateral force and the PSPD output in (5) becomes

$$f_\eta = \text{sgn}(\eta)\alpha_l \hat{V}_\eta^{(l)}. \quad (7)$$

However, in general, this calibration requires a very large tilt of the AFM head with respect to the scanning plane of the substrate. In most cases, we use the AFM with an alignment such that the top surface of the AFM thin film cantilever is parallel to the scanning plane. For such a setup, the force components in the  $(x, y)$  coordinates,  $\{-\text{sgn}(\eta)f_\eta, N_\eta\}$ , in (5) can be expressed in terms of the components in the  $(\hat{x}, \hat{y})$  coordinates,  $\{-\text{sgn}(\eta)\hat{f}_\eta, \hat{N}_\eta\}$ , using the orthogonal transformation matrix

$$\begin{bmatrix} N_\eta \\ f_\eta \end{bmatrix} = \begin{bmatrix} \cos \phi^* & \text{sgn}(\eta)\sin \phi^* \\ -\text{sgn}(\eta)\sin \phi^* & \cos \phi^* \end{bmatrix} \begin{bmatrix} \hat{N}_\eta \\ \hat{f}_\eta \end{bmatrix}. \quad (8)$$

Then, substituting (8) into (5), we arrive at

$$\hat{f}_\eta = \text{sgn}(\eta)\{\alpha_{ll}\hat{V}_\eta^{(l)} + \alpha_{ln}\hat{V}_\eta^{(n)}\}, \quad (9a)$$

where we used the normal system response relationship

$$\hat{N}_\eta = \alpha_n \hat{V}_\eta^{(n)} \quad (9b)$$

with the *normal force constant*  $\alpha_n$ , the *lateral force constant*  $\alpha_{ll}$  and the *crosstalk lateral force constant*  $\alpha_{ln}$ , for which

$$\alpha_{ll} = \alpha_l\{(1 - \xi)\cos \phi_m + \xi \cos \phi^*\}, \quad (10a)$$

$$\alpha_{ln} = \alpha_n\{(1 - \xi)\sin \phi_m + \xi \sin \phi^*\}/\{(1 - \xi)\cos \phi_m + \xi \cos \phi^*\}. \quad (10b)$$

In (9b) the crosstalk normal force constant  $\alpha_{nl}$  does not appear because the component of the lateral force in the direction of the cantilever axis is negligible. Therefore, it is reduced to calibrating the three force constants,  $\alpha_n$ ,  $\alpha_{ll}$ , and  $\alpha_{ln}$ , for complete characterization of the mechanical responses of the AFM cantilever-tip assembly. When  $\phi_m = 0$  and  $\phi^* = 0$ , as a special case,  $\alpha_{ln}$  vanishes and  $\alpha_{ll}$  reduces to the calibration constant  $\alpha$  used by Varenberg *et al.*<sup>7</sup>

Except for special slope tests such as employed in W-LFC,<sup>4</sup> AFM friction tests are generally carried out with the substrate angle  $\phi^* = 0$ , for which the transformation matrix in (8) becomes the identity matrix and the force components in the sensing coordinates are identical to the components in the friction coordinates, i.e.,  $\hat{f}_\eta = f_\eta$  and  $\hat{N}_\eta = N_\eta$ . In a typical AFM friction experiment with  $\phi^* = 0$ , a friction loop composed of forward sliding and backward sliding processes, under constant normal load, is used to get rid of the effect of the crosstalk force constant  $\alpha_{ln}$  in (9a). By adding (9a) for  $\eta = a$ , and  $b$ , we have

$$\bar{f} = \alpha_{ll}\hat{w}, \quad (11)$$

where  $\bar{f} = (f_a + f_b)/2$  is the average friction for the forward and backward sliding processes and  $\hat{w} = \{\hat{V}_a^{(l)} - \hat{V}_b^{(l)}\}/2$  is the loop width of the lateral PSPD output. For such experiments, the system response constant is related to the other variables as

$$\alpha_{ll} = \kappa/[\beta_l H\{(1 - \xi)\cos \phi_m + \xi\}]. \quad (12)$$

While this technique of removing the crosstalk effect has been widely used, it is insufficient to measure absolute values of friction forces which depend on slip directions. Therefore, we provide a complete and direct method of measuring  $\alpha_{ln}$  as well as  $\alpha_{ll}$  in this article.

## B. Difficulties and limitations in existing calibration techniques

Calibrating the force constants,  $\alpha_{ll}$ ,  $\alpha_{ln}$ ,  $\alpha_n$ , and  $\alpha_l$ , based on (7) and (9), regarding the  $\alpha$ 's as constants of the system response, is a direct method of calibration. Calibrating the force constants based on (6) and (10), evaluating the variables on the right hand sides of the equations separately, is an indirect method of calibration. For indirect methods we have to evaluate three AFM cantilever-tip characteristics. For example, the lateral force constant  $\alpha_l$  is comprised of a deformation characteristic  $\kappa$ , an intermediate transducer characteristic  $\beta_l$ , and a structural geometry characteristic  $H$  of the

cantilever-tip assembly, as shown in (6). So far, any existing technique for calibrating the force constants could either be characterized as an indirect method of calibration<sup>8-12</sup> or as a semidirect method of calibration.<sup>4,7</sup> The wedge method<sup>4</sup> is one such semidirect calibration method, because we have to evaluate separately some geometric variables, in general, for  $\xi \neq 0$ , although we do not have to assess the torsional spring constant and the angle sensitivity constant individually. In this section we will discuss some difficulties and limitations in calibrating the force constants with existing methods.

Evidently the indirect method has three error sources. One is in the estimation of the torsional spring constant  $\kappa$  of the cantilever, another in assessing the effective cantilever-tip structural geometry parameters ( $H, \xi, \phi_m$ ), and the last, in gauging the angle sensitivity constant  $\beta_l$  of the PSPD. The torsional spring constant  $\kappa$  can be expressed in terms of the elastic moduli and geometric dimensions of the cantilever in theory.<sup>8-11</sup> However, computational or analytical estimation of the spring constant of the thin film cantilever structure is inaccurate and the use of the calculated value is not practical. Distribution of the elastic moduli of the submicron thick cantilever material is not uniform at the small scale, in general. Cantilevers are often metallized and the effect of metallization on the cantilever spring constant can be significant.<sup>13</sup> The oxide layer and the surface roughness also affect the spring constant. In general, the thickness of an AFM cantilever is not really uniform and the cantilever is not straight in its relative dimension. Nevertheless, the torsional spring constant or its ratio to normal spring constant has been estimated with various models of linear elastic analysis.<sup>8-11</sup> In order to overcome these difficulties, attempts have been made to measure the torsional spring constant experimentally.<sup>13,14</sup>

Even if the spring constant could be estimated reasonably, evaluations of the geometric variables ( $H, \xi, \phi_m$ ) are most uncertain in assessing the force constants with the indirect methods. Albeit the dimensions of the cantilever-tip assembly could be measured precisely with a very good scanning electron microscope, the location of the shear center,  $C$  in Fig. 1, of a beam which is curved slightly or has an uneven property distribution can be far from the midpoint of the thin film cross section near the tip. In addition, estimation of  $\xi$  and  $\phi_m$  is also nontrivial. Furthermore, it has been noticed that the accuracy of the angle sensitivity constant  $\beta_l$  of the PSPD depends on the laser alignment and photodetector sensitivity significantly.<sup>4,9</sup> In many cases, the indirect method erroneously determines the force constants to be an order of magnitude away from their actual value. Thus, calibration of the force constants based on an indirect method is very difficult and ineffective.

Next we consider a semidirect method of calibration, known as the wedge method. Ogletree *et al.*<sup>4</sup> developed the wedge method for a calibration of the lateral force constant,  $\alpha_{ll}$ , circumventing the difficulties of evaluating the variables involved in the indirect methods. The calibration was accomplished by sliding the tip across surfaces of two different slopes,  $\phi_{\pm}^*$ , with  $\pm$  indicating the two different wedge faces, and measuring the PSPD outputs  $\hat{V}_{\eta}^{(l)}$  of critical slips at different levels of  $\hat{N}$ . The basic principle of this calibration can

be understood as follows. If the parametric functional form of the friction law, e.g.,  $f_{\eta}(N_{\eta}; \mathbf{q}_{\eta})$  with parameters  $\mathbf{q}_{\eta}$  is known, the measurement of  $f_{\eta}(\phi^*; \phi_m, \xi, \alpha_l)$  and  $N_{\eta}(\phi^*; \phi_m, \xi, \alpha_l)$  for various  $\phi^*$  can be used to get the best fit values of the parameters  $\mathbf{q}_{\eta}$ ,  $\phi_m$ ,  $\xi$ , and  $\alpha_l$ . The differential friction coefficient  $\mu$  and the adhesion parameter  $A$  of Ogletree *et al.*<sup>4</sup> are examples of the parameters  $\mathbf{q}_{\eta}$ . The minimum necessary number of independent measurement data sets ( $f_{\eta}, N_{\eta}$ ) for different  $\phi^*$  is the number of total parameters to determine the unknown parameters with the best fit process. Once the parameters are determined, the lateral force constant  $\alpha_{ll}$  can be found with (9a) in terms of the parameters. Ogletree *et al.*<sup>4</sup> used well-defined crystallographic surfaces of the wedge to minimize uncertainties in measuring  $\phi^*$ .

However, this method has several issues: (A) This method has to employ frictional sliding processes to use a friction law, e.g.,  $f_{\eta}(N_{\eta}; \mathbf{q}_{\eta})$ ; (B) since the friction law exhibits approximately a characteristic of piecewise linearity, the large number of data sets for a wide range of  $\hat{N}_{\eta}$  has only four independent relationships to determine the parameters involved in the friction process, and thus the total number of unknown parameters cannot exceed 4; and (C) if we treat the shear center misalignment properly, the geometric variables  $\phi_m$  and  $\xi$  have to be evaluated to determine  $\alpha_{ll}$  through complicated data processing, although, unlike other indirect methods, the torsional spring constant  $\kappa$  and the geometric variable  $H$  do not have to be estimated explicitly.

Regarding the problem of (A), since the calibration relies on frictional slip processes over sharp edges of the wedge, the tip can be subjected to wear damage during the calibration process as pointed out by Cain *et al.*<sup>15</sup> Also the critical friction forces at the onset of slip have stochastic features and it is difficult to read such forces accurately. With regard to (B), it is convenient to use a difference form of (5), and the corresponding comprehensive analysis of an AFM response in the wedge method is summarized in Appendix A. Defining the differential friction coefficient  $f'_{\eta} = \Delta f_{\eta} / \Delta N_{\eta}$  in general we have seven parameters,  $f'_{\eta\pm}$ ,  $\phi_m$ ,  $\xi$ , and  $\alpha_l$ , to be determined with the four independent relationships. Therefore, Ogletree *et al.*<sup>4</sup> assumed that the friction is independent of the slip directions so that the frictional responses for the forward and backward slips are the same, i.e.,  $f'_{a\pm} = f'_{b\pm}$ . This could reduce the unknowns to five. Furthermore, they assumed that the tip is ideally sharp, i.e.,  $\xi=0$ , to solve the problem. Considering (C), the geometric variables  $\phi_m$  and  $\xi$  have to be evaluated explicitly, in general, and therefore, the wedge method is not truly a direct method. The wedge method has an additional technical limitation on the size of the tip radius. For example, in the study of Ogletree *et al.*,<sup>4</sup> the wedge method could be only applied to tips with radii less than 100 nm because of the short (10–100 nm) spacing between SrTiO<sub>3</sub> (305) surface ridge crests of the calibrating wedge.

The wedge method was extended by Varenberg *et al.*<sup>7</sup> to handle the probes with large radii, i.e.,  $\xi \neq 0$ , but practically smaller than 2  $\mu\text{m}$ . However, they assumed that  $\phi_m$  is zero in their derivations,<sup>7</sup> and it is not an accurate assumption for general colloid probes. A few microns offset of the shear center can completely break down the validity of the uphill

and downhill moments in their equation [(7) and (8)].<sup>7</sup> Furthermore, since the torsion loop offset is crucial for their improved wedge method, Varenberg *et al.*<sup>7</sup> tried to use a flat facet to cancel the crosstalk effect. But their assumption that *on the flat surface the torsion loop offset must be equal to zero* is not correct for  $\phi_m \neq 0$ . The torsion loop offset varies with the normal load, in general, due to the crosstalk effect. Moreover, the Eqs. (A3) and (A4) in our analysis show that by simple subtraction the crosstalk effect cannot be ruled out if  $\xi \neq 0$ . For these reasons the lateral force constants calibrated by the W-LFC method are compared with those of the D-LFC method *only for sharp tips* in the following section.

Finally, it is worth mentioning that many indirect and semidirect methods of lateral force calibration depend on knowledge of the normal spring constant, which has some uncertainties. The current state of the art technique provides approximately 10% accuracy in measuring the normal force constant with a direct method of calibration.<sup>16</sup> The direct method usually employs another lever of known spring constant or a microfabricated array of reference springs (MARS) for the calibration.<sup>16</sup> In this article, a novel *in situ* direct method is developed to independently calibrate the lateral force constant. It correlates the output voltage signals from a PSPD directly to the lateral force applied on the AFM cantilever assembly by a diamagnetic levitation spring system. This method is relatively easy to implement and has great sensitivity to small lateral forces at the nano-Newton scale.

## II. D-LFC: A DIRECT METHOD OF CALIBRATING THE FRICTION FORCE CONSTANTS

In this section, we present a direct method of calibrating the lateral force constants of an AFM cantilever-tip system, which leads to the development of a D-LFC. For this development, we noticed that most AFM thin film cantilevers have typical lateral spring constants on the order of 100 nN/nm and an operational range well within 100 nm of deflection. Thus, a compliant load cell with a spring constant of about 10 pN/nm can calibrate the AFM force constants accurately with a few micrometers of a spring displacement of the load cell. Such a compliant load cell, small enough to be adapted to most AFM systems, can be made simply with a diamagnetic levitation spring. We start this section with a description of such a spring load cell system.

### A. A diamagnetic levitation spring system

It is known that a diamagnetic material such as a graphite sheet can be levitated in a magnetic field and behaves like a spring system. The levitated graphite sheet has negligible air and eddy-current drag due to its slow motion, and the spring constants of the system can be tuned quite small in magnitude. These two important features make the system attractive for the calibration of AFM force constants as will be clearly described in the rest of this article.

In a diamagnetic substance the magnetic moment induced by an applied magnetic field opposes the applied magnetic field and the substance repels the source of the magnetic field, e.g., magnet, exhibiting negative susceptibility. Many substances including water, protein, carbon, DNA,

TABLE I. Values of susceptibility  $\chi$  for various diamagnetic materials (in SI units).

Material	$\chi (\times 10^{-6})$
Water	-8.8
Gold	-34
Bismuth metal	-170
Graphite rod	-160
Pyrolytic graphite $\perp$	-450
Pyrolytic graphite $=$	-85

plastic, wood, graphite, and bismuth are diamagnetic.<sup>17</sup> Susceptibilities of some diamagnetic materials are summarized in Table I. Among them, graphite and bismuth display very strong diamagnetism. The susceptibility of a chemical-vapor deposition (CVD)-grown pyrolytic graphite (PG) is highly anisotropic and the susceptibility in the direction perpendicular to the basal plane is several times higher than that in the direction parallel to the plane. This strong anisotropy is useful in suspending a PG sheet in a magnetic field, balancing the gravity force, while the lateral spring constant of levitation is tuned to be small. Properties of a diamagnetic levitation spring system are explained as follows.

The body force per unit volume,  $\mathbf{f}^{(m)}$ , exerted on a PG sheet in a magnetic field of flux density  $\mathbf{B}$  is given as

$$\mathbf{f}^{(m)} = \nabla(\boldsymbol{\mu} \cdot \mathbf{B}), \quad (13)$$

where  $\boldsymbol{\mu} = \boldsymbol{\chi} \cdot \mathbf{B} / \mu_0$  is the magnetic dipole moment per unit volume, with  $\boldsymbol{\chi}$  the molecular susceptibility tensor of PG and  $\mu_0$  the permeability of the vacuum. Then, the net magnetic force  $\mathbf{F}^{(m)}$  and the magnetic moment  $\mathbf{M}^{(m)}$  applied at the mass center of the PG sheet are expressed as

$$\mathbf{F}^{(m)} = \frac{1}{\mu_0} \int_{V(\mathbf{y})} \nabla_{\mathbf{x}} \{ \mathbf{B}(\mathbf{x}) \cdot \boldsymbol{\chi} \cdot \mathbf{B}(\mathbf{x}) \} dV, \quad (14a)$$

$$\mathbf{M}^{(m)} = \frac{1}{\mu_0} \int_{V(\mathbf{y})} (\mathbf{y} + \boldsymbol{\Omega} \times \mathbf{y}) \times \nabla_{\mathbf{x}} \{ \mathbf{B}(\mathbf{x}) \cdot \boldsymbol{\chi} \cdot \mathbf{B}(\mathbf{x}) \} dV, \quad (14b)$$

where  $\mathbf{x} = \mathbf{x}^{(0)} + \mathbf{y} + \boldsymbol{\Omega} \times \mathbf{y}$ , with  $V(\mathbf{y})$  the volume of the PG sheet,  $\mathbf{x}^{(0)}$  the position of the mass center of the PG sheet,  $\mathbf{y}$  a position vector with respect to the mass center, and  $\boldsymbol{\Omega}$  an infinitesimal rotation vector of PG. Then, the force balance  $\mathbf{F}^{(m)} - m^{(L)} g \mathbf{e}_3 = \mathbf{0}$  and the moment balance  $\mathbf{M}^{(m)} = \mathbf{0}$  determine the equilibrium position and rotation of  $\mathbf{x}^{(0)}$  and  $\boldsymbol{\Omega}$ . Here,  $m^{(L)}$  is the mass of levitation,  $g$  the gravitational acceleration, and  $\mathbf{e}_3$  the vertical upward unit vector. The components of the translational spring constant tensor  $k_{ij}^{(m)}$  and the angular spring constant tensor  $\kappa_{ij}^{(m)}$ , for  $i$  and  $j=1, 2, \text{ or } 3$ , can be evaluated with the following differentiations at the equilibrium point:

$$k_{ij}^{(m)} = \frac{\partial F_i^{(m)}}{\partial x_j^{(0)}}, \quad (15a)$$

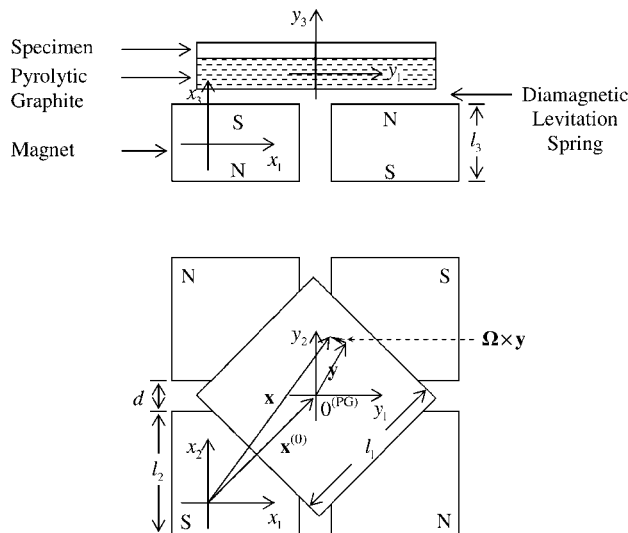


FIG. 2. Diamagnetic levitation load cell of the D-LFC:  $(x_1, x_2, x_3)$  are the magnet coordinates,  $(y_1, y_2, y_3)$  the levitated-mass coordinates, and  $\Omega$  the rotation vector of the levitated mass.

$$\kappa_{ij}^{(m)} = \frac{\partial M_i^{(m)}}{\partial \Omega_j} \quad (15b)$$

Since the moment is defined with respect to the mass center, the translational and the angular spring constant tensors are decoupled.

An effective design of a diamagnetic levitation load cell system is illustrated in Fig. 2. In this design a square sheet of pyrolytic graphite is levitated in the magnetic field of four permanent magnets arranged as shown in the figure. The material of interest for the AFM friction test, e.g., a mica sheet, is mounted on the top surface of the PG sheet. In this arrangement the principal axes of the spring constant tensors can be aligned closely with  $(y_1, y_2, y_3)$  axes shown in the figure. Adjusting the gap distance  $d$  between the magnets for a given ratio of  $l_2/l_1$ , we can control the ratios between the principal values of the spring constants. For example, it is desirable to have the calibration of the AFM lateral force constants under the conditions of  $k_I \approx k_{II} \ll k_{III}$  and  $\kappa_I \approx \kappa_{II} \gg \kappa_{III}$ , which can be achieved by choosing  $l_1/l_2 \approx \sqrt{2}$  and  $d/l_1 \ll 1$ . Then, the spring displacement should be within a range of  $\pm d$ . By adjusting the shape of the PG sheet and the gap distance  $d$ , we can create a magnetic levitation spring system to calibrate not only the lateral AFM force constant  $\alpha_{II}$ , but also the normal constant  $\alpha_n$  and the crosstalk constant  $\alpha_{In}$  simultaneously. This nearly friction-free system creates an ideal load cell for calibrating an AFM cantilever-tip assembly. With four 4.76 mm cubic Nickel-plated neodymium iron boron (NdFeB) magnets of grade N38 ( $BH_{\max} = 38$  MG Oe) we could make a lateral force load cell operating in a range from a few nanonewtons to a few micronewtons, with the spring displacement range well within  $\pm 100 \mu\text{m}$  approximately. Once the lateral spring constant of this levitation system is determined, a direct correlation between the applied lateral force and the resulting output voltage signals from the AFM PSPD can be established without ambiguity. The details of the vibration characteristics and the

compliances of the system will be discussed in the next subsection.

## B. Free vibration characteristics and the spring constants of the levitation system

Typically, spring constants of a system can be evaluated by measuring the natural vibration frequencies of the system. General vibration characteristics of the diamagnetic levitation system are provided in Appendix B. As discussed in the Appendix, there are six eigenfrequencies of levitation-vibration. However, as we mentioned in the previous section, we designed the levitation system to have the principal directions aligned with  $(y_1, y_2, y_3)$  axes. We also use a laser displacement tracer system only sensitive to the displacement in a lateral, say,  $x_1$  direction. Then, the equation of free vibration in the  $x_1$  direction can be reduced from (B2a) to

$$\ddot{x}_1 + 2\zeta\omega_n\dot{x}_1 + \omega_n^2 x_1 = 0, \quad (16)$$

where  $\zeta = c_{11}/(2\sqrt{m^{(L)}k_{11}})$  and  $\omega_n = \sqrt{k_{11}/m^{(L)}}$ . The general solution of the equation is

$$x_1(t) = e^{-\zeta\omega_n t} (a_1 \sin \omega_d t + a_2 \cos \omega_d t), \quad (17)$$

where  $\omega_d = \omega_n \sqrt{1 - \zeta^2}$ , with coefficients  $a_1$  and  $a_2$  to satisfy the initial conditions. Thus, the spring constant  $k_{11}$  can be evaluated by

$$k_{11} = m^{(L)} \omega_n^2 = m^{(L)} \omega_d^2 / (1 - \zeta^2). \quad (18)$$

Figure 3(a) shows a typical measurement of the free vibration amplitude as a function of time for the diamagnetic levitation system for the sample listed as PG-1 in Table II. Data analyses (see Table II) show that the diamagnetic levitation spring system has the damping parameter  $\zeta$  on the order of  $10^{-2}$  and  $|(\omega_n^2/\omega_d^2) - 1| \sim 10^{-4}$ . Thus, the approximation  $k_{11} \approx m^{(L)} \omega_d^2$  has a relative error of the stiffness measurement on the order of  $10^{-4}$ . Figure 3(b) exhibits the frequency spectrum of free vibration signal of the sample PG-1, from which we can read the dynamic frequency  $\omega_d$  readily. The frequency can be then converted to the spring constant  $k_{11} \approx m^{(L)} \omega_d^2$ . The typical spring constant of our levitation system is on the order of 10 pN/nm as shown in Table II. Further details of our calibration system will be discussed in Sec. III A. An additional remark for measuring the natural frequency is that the  $x_1$  direction has to be aligned with the direction of the lowest frequency mode of vibration if the eigenfrequencies are quite distinct. Otherwise, the intermediate frequency mode is unstable and the frequency measurement in the direction of the intermediate vibration mode can be inaccurate.

## C. Principles of the D-LFC

Once the spring constant  $k_{11}$  of the diamagnetic levitation spring system is evaluated, it can be used to calibrate the AFM lateral force constants  $\alpha_{II}$  and  $\alpha_{In}$ . A schematic of the calibration setup is shown in Fig. 4(a). In the setup, the diamagnetic levitation system is mounted on the stage of the AFM base scanner, and a specimen of interest is glued on top of the levitating pyrolytic graphite sheet as shown in the figure. For the calibration, once the AFM tip is engaged on the specimen surface, the magnets together with the AFM

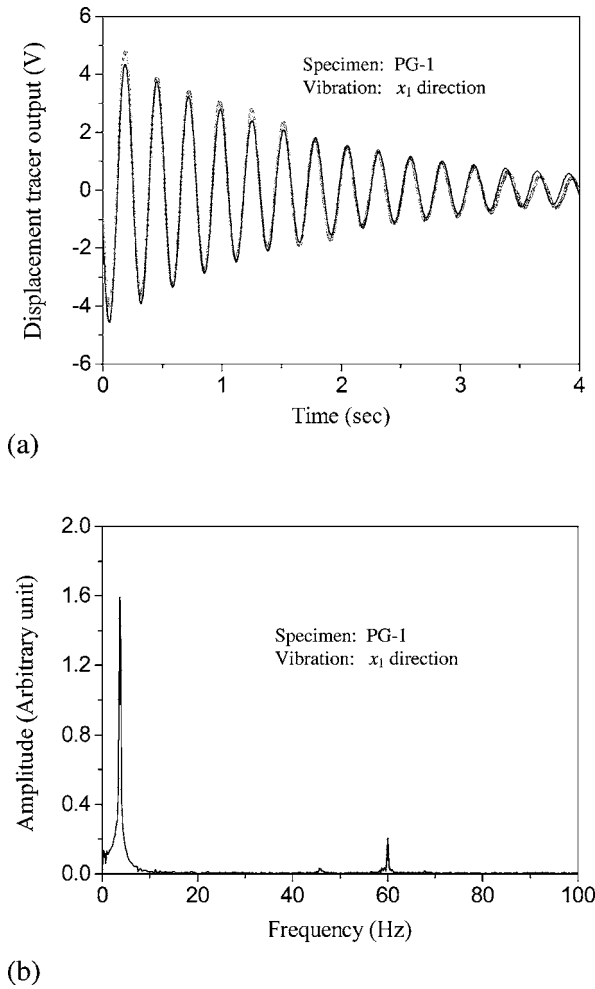


FIG. 3. (a) Time trace of the free vibration amplitude for PG-1. (b) Frequency spectrum of the PG-1 vibration.

base are reciprocated by the lateral scanner, while the normal load  $\hat{N}$  is held fixed by holding the normal PSPD output  $\hat{V}^{(n)}$  constant through the feedback controller. Then, the lateral PSPD output  $\hat{V}^{(l)}$  is recorded against the lateral base dis-

placement  $\Delta x_1^{(b)}$ . The displacement  $\Delta x_1^{(b)}$  is related to the lateral force  $f$  by

$$f = k_{11}\Delta x_1^{(m)} \approx k_{11}\Delta x_1^{(b)}, \quad (19)$$

where the base displacement can be decomposed,  $\Delta x_1^{(b)} = \Delta x_1^{(m)} + \Delta x_1^{(t)}$ , into the displacements of the magnetic spring  $\Delta x_1^{(m)}$  and the AFM tip  $\Delta x_1^{(t)}$ . The tip displacement  $\Delta x_1^{(t)}$  is caused by the compliance of the tip contact and the cantilever twist. It is typically within a few nanometers, while the magnetic spring displacement is on the order of tens of micrometers. Therefore, the tip displacement can be neglected in (19). In this calibration procedure, the maximum reciprocating displacement of the lateral base displacement  $\Delta x_1^{(b)}$  is limited to induce a lateral force  $f$  well within the static friction force of the onset of slip. In contrast to the wedge method the AFM tip does not slip in this direct method of calibration.

Figure 4(b) shows an experimental measurement of the lateral PSPD output against the lateral displacement of the magnets on the AFM base reciprocated within  $\pm 25 \mu\text{m}$  for contact between a mica specimen mounted on a levitated PG sheet (PG-2 in Table II) and a spherical bead attached near the end of an AFM cantilever (NCD in Table III). The bead is made of borosilicate glass coated with a 50 nm gold layer and has a diameter of  $15 \mu\text{m}$ . The experimental data show that the response is linear and reversible within the thermal and feedback noise bands for forward and backward scanning of the base displacement. While further details of more experimental results will be presented in Sec. III B, the principles of the measurement of the AFM force constants  $\alpha_{ll}$  and  $\alpha_{ln}$  are presented here as follows.

To simplify data processing, the AFM base displacement in this setup is approximated as the lateral spring displacement as discussed above. Then, it is multiplied by the spring constant  $k_{11}$  and converted to the lateral force  $f$ , which is marked on the horizontal axis at the top of Fig. 4(b). Now, we have a data set relating  $\hat{f}$  and  $\hat{V}^{(l)}$  for a fixed value of  $\hat{V}^{(n)}$ . Recalling (9a) in a difference form,  $\Delta \hat{f} = \alpha_{ll}\Delta \hat{V}^{(l)} + \alpha_{ln}\Delta \hat{V}^{(n)}$ ,

TABLE II. Characteristics of the pyrolytic graphite diamagnetic levitation spring systems.

Specimen	Dimension (mm)	Mass (mg)	Axis	$\omega_n$ (rad/s)	$\zeta$	$k_{11}$ (pN/nm)
PG-1	5.57 × 5.54 × 0.35	15.052	$x_1$	23.621	0.024 06	8.3983
			$x_2$	32.530	0.016 50	15.928
PG-2	5.28 × 5.16 × 0.54	22.111	$x_1$	35.946	0.015 82	28.570
			$x_2$	34.213	0.014 48	25.882
PG-3	4.13 × 4.15 × 0.47	11.470	$x_1$	44.491	0.016 40	22.704
			$x_2$	44.363	0.008 66	22.574
PG-4	5.81 × 5.87 × 0.59	25.321	$x_1$	28.343	0.018 75	20.341
			$x_2$	22.578	0.028 82	12.908
PG-5	5.21 × 5.20 × 0.51	21.061	$x_1$	35.748	0.014 36	26.914
			$x_2$	34.145	0.014 68	24.555
PG-6	2.89 × 2.75 × 0.28	2.9110	$x_1$	50.739	0.013 93	7.4942
			$x_2$	60.437	0.010 77	10.633

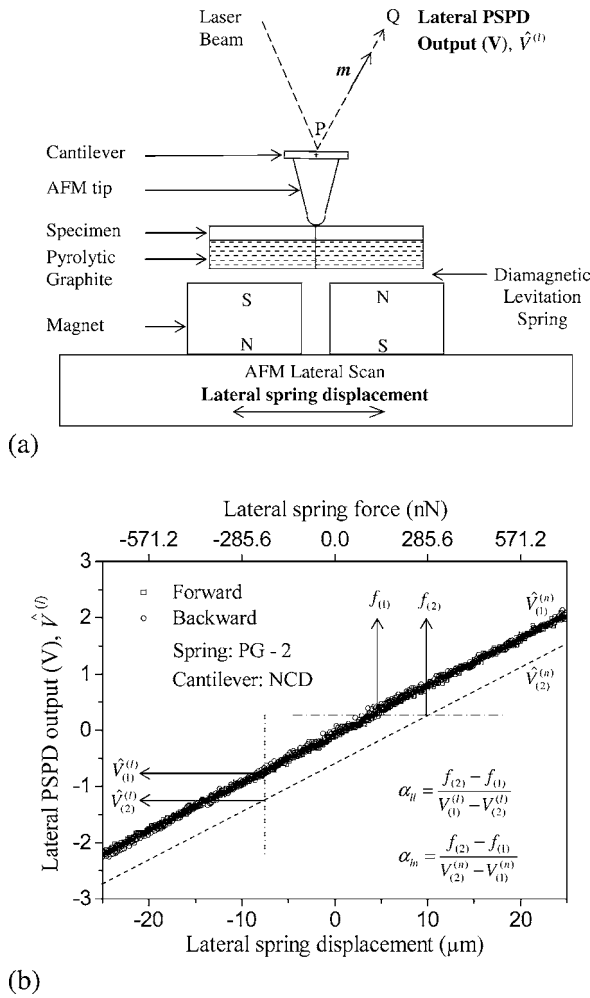


FIG. 4. (a) A schematic of the D-LFC. (b) A diagram showing the D-LFC principles for measuring the force constants  $\alpha_{||}$  and  $\alpha_{\perp}$ : the data set was collected with the PG-2 diamagnetic spring for the NCD AFM cantilever-bead assembly.

the inverse slope,  $\partial f / \partial \hat{V}^{(l)}$ , of the data is the lateral force constant  $\alpha_{||}$ . In addition, two response lines for two different  $\hat{V}^{(n)}$ 's, for example,  $\hat{V}_{(1)}^{(n)}$  and  $\hat{V}_{(2)}^{(n)}$  shown in Fig. 4(b), should be parallel to each other as shown by a dashed line in the figure. The inverse slope  $\alpha_{||}$  can also be represented by the ratio between the horizontal offset  $f_{(2)} - f_{(1)}$  and the vertical offset  $\hat{V}_{(1)}^{(l)} - \hat{V}_{(2)}^{(l)}$  of the two parallel lines, i.e.,  $\alpha_{||} = \{f_{(2)} - f_{(1)}\} / \{\hat{V}_{(1)}^{(l)} - \hat{V}_{(2)}^{(l)}\}$ , as shown in the figure. Furthermore, the crosstalk lateral force constant  $\alpha_{\perp}$  is given by  $\alpha_{\perp} = \partial f / \partial \hat{V}^{(n)}$  and the relationship becomes  $\alpha_{\perp} = \{f_{(2)} - f_{(1)}\} / \{\hat{V}_{(2)}^{(n)} - \hat{V}_{(1)}^{(n)}\}$  for the linear system. Thus, experimental measurements of the responses  $\hat{V}^{(l)}$ 's with respect to the lateral force (or spring displacement) for two different  $\hat{V}^{(n)}$ 's can provide the values of both  $\alpha_{||}$  and  $\alpha_{\perp}$ . In real calibrations the responses are recorded for many different  $\hat{V}^{(n)}$ 's, and all data sets are used to get  $\alpha_{||}$  and  $\alpha_{\perp}$  with a least squares fit, minimizing

$$\Psi(\alpha_{||}, \alpha_{\perp}, \hat{f}_0) = \sum_{k=1}^N \{\hat{f}_k - [\alpha_{||} \hat{V}_k^{(l)} + \alpha_{\perp} \hat{V}_k^{(n)} + \hat{f}_0]\}^2. \quad (20)$$

Experimental values of the lateral force constants measured with this method are provided in Table III and discussed

TABLE III. Force constants  $\alpha_{||}$  and  $\alpha_{\perp}$  measured by D-LFC for different AFM cantilever types.

Cantilever				
Type	Contact	Coating	$\alpha_{  }$ (nN/V)	$\alpha_{\perp}$ (nN/V)
NCD <sup>d</sup>	Bead	Au	320.68 ± 2.19	-17.83 ± 0.59
NCD	Bead	Au	333.04 ± 2.28	Not measured
NCB <sup>1</sup>	Bead	Al	97.68 ± 0.15	Not measured
NCB <sup>2</sup>	Bead	Al	69.52 ± 0.18	Not measured
NCC <sup>d</sup>	Tip	Au	602.01 ± 6.88	-96.51 ± 1.36
NCC*	Tip	Au	591.92 ± 0.25	Not measured
CTB*	Tip	None (Si)	49.61 ± 0.13	Not measured

further in Sec. III C for various AFM cantilevers.

### III. EXPERIMENTS

We have established the working principles of the D-LFC in the previous section, and we present the experimental results in this section. The experimental results include measurements of the D-LFC system spring constant, calibration of the lateral force constants for various AFM cantilever-tip and -bead assemblies, and comparisons between the lateral force constants measured by the D-LFC and the W-LFC, respectively.

#### A. Spring-constant measurement of the diamagnetic levitation system

The diamagnetic levitation calibrator system consists of four, 4.76 mm cubic magnets described in Sec. II A and a pyrolytic graphite sheet from scitoys.com. The pyrolytic graphite sheets were cleaved and cut into different sizes using a razor blade, then each of them was glued to a thin sheet of muscovite mica, obtained from SPI® supplies. Finally, these mica sheets are cleaved in air and each composite sheet of mica and PG was weighed by a microbalance (Mettler Toledo® MX5). The dimension was measured by a digital Vernier caliper with an accuracy of 10 μm. The dimension and mass measurements of six different PG specimens are shown in Table II. The dimensions of the PG specimens span from about 3 × 3 × 0.3 mm<sup>3</sup> to 6 × 6 × 0.6 mm<sup>3</sup> and the masses of the specimens range from about 3 to 25 mg. The PG specimen is then levitated in the magnetic field, and the free vibrations of the PG specimens in the  $x_1$  and  $x_2$  directions are measured with a laser displacement detection system. All of the following calibrations were done on an AutoCP AFM system from Park Scientific Instruments.

For the measurement of the free vibration amplitude, a sheet of a 10 mW He-Ne laser light was partially blocked by the edge of the PG vibrating in the  $x_1$  direction. Then, the transmitted-light intensity was detected by a photodiode. The time trace of the amplitude is shown in Fig. 3(a) for PG-1 vibrating in the  $x_1$  direction. The trace indicates that the light intensity distribution in the cross section of the laser light sheet seems to be slightly uneven, so that the measured amplitude of the photodetector output is slightly biased upward for the large amplitude in the figure. Nevertheless, the linear solution (17) fits the experimental data well for its frequency

measurement and thus the spring constant. A fast Fourier transform (FFT) was carried out for the signal and the result is shown in Fig. 3(b). Two major peaks are observed in the frequency domain. One corresponds to the free vibration of the PG sheet and the other the electric noise at 60 Hz. With the same procedure, six different nearly square PG sheets were tested and the vibration characteristics are reported in Table II. For the signal processing a low-pass filter was utilized to remove the 60 Hz noise before every signal is best fitted to (16) to get the values of  $\omega_n$  and  $\zeta$  as reported in Table II. It was noticed that, in general, vibration along one diagonal direction is more stable than the other, and the stable direction was used for subsequent calibration processes. As mentioned earlier, the intermediate mode of vibration is unstable and the separation of the vibration modes in  $x_1$  and  $x_2$  for the nearly square sheets of the specimens PG-1 and PG-4 may be caused by the asymmetric distribution of pyrolytic graphite grain orientations and the slight asymmetry of the sample shape. The lateral spring constants,  $k_{11}$ , of the diamagnetic levitation system with six differently sized PG specimens ranged from 7.5 to 29 pN/nm.

### B. D-LFC measurement of the AFM lateral force constants

After the lateral magnetic spring constant  $k_{11}$  is obtained, the rest of the calibration procedure is just like performing a usual AFM friction measurement with a conventional substrate replaced by the diamagnetic levitation calibrator system. Details of the technical procedure follow the steps described in Sec. II C. For the experiments, we used AFM cantilever-bead as well as cantilever-tip assemblies. The AFM cantilever-bead assembly is composed of a stiff non-contact (NC) mode AFM cantilever purchased from Veeco Inc. and a spherical borosilicate glass bead of 15  $\mu\text{m}$  diameter, attached near the end of the cantilever. The cantilever types are further classified as A, B, C, and D types depending on the width, length, and thickness of the cantilever. For example, a noncontact mode C-type cantilever is denoted NCC in Table III. Its nominal normal spring constant is 13 nN/nm. In contrast, the AFM cantilever-tip assembly consists of an AFM cantilever of either a NC or a contact (CT) mode type, and a usual AFM tip of a silicon apex made by chemical etching. The contact mode cantilever is relatively compliant. For example, the CTB cantilever has a nominal normal spring constant of 0.4 N/m. The tips and beads are either bare or coated with a 50 nm thin film layer of gold or aluminum. The coating layer is also indicated in Table III.

Figure 5(a) shows plots of the lateral PSPD output  $\hat{V}^{(l)}$  against the variation of the lateral spring displacement  $x_1$  for 15  $\mu\text{m}$  strokes for five different values of  $\hat{V}^{(n)}$  measured with a cantilever-bead assembly on the PG-2 spring system. The cantilever is listed as NCD<sup>d</sup> in Table III. The normal loads were prescribed by five different fixed values of  $\hat{V}^{(n)}$  in equal increments of  $-1.587$  V corresponding to a nominal increment of 200 nN in  $\hat{N}$ , using the feedback control of the AFM normal loading. It is noticed that  $\alpha_n$  in (9b) has a negative value for our AFM system. The plot shows five parallel lines

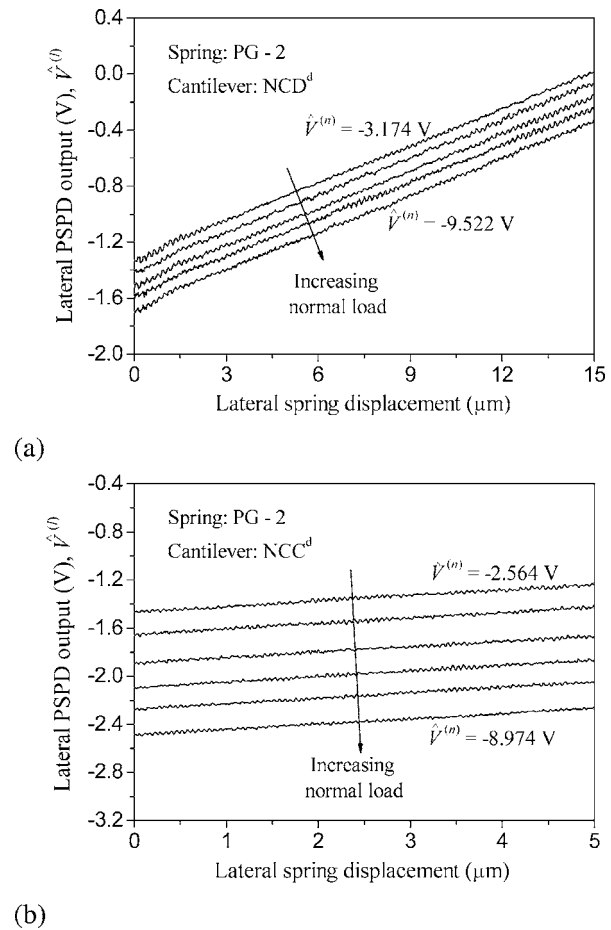


FIG. 5. D-LFC data of the lateral PSPD output showing a linear dependence on the lateral spring displacement under incremental normal loads (a) for the NCD<sup>d</sup> cantilever-bead and (b) for the NCC<sup>d</sup> cantilever-tip assemblies.

superposed with some noise. We believe that it is mainly caused by thermal vibrations and the circuit noise of the normal-loading feedback control. Small deviations of the five lines from straightness are also observed near the left end of the lines,  $0 \leq x_1 < 1.5$   $\mu\text{m}$ . This anomaly is believed to be an effect of a small nanometer scale bump either on the surface of the gold coating or on the mica surface. Figure 5(b) exhibits similar plots of six lines for the cantilever-tip assembly listed as NCC<sup>d</sup> in Table III. This measurement was made for a spring-displacement stroke of only 5  $\mu\text{m}$  on the PG-2 spring system, with six different fixed values of  $\hat{V}^{(n)}$  in equal increments of  $-1.282$  V corresponding to a nominal increment of 100 nN in  $\hat{N}$ . This corresponds to applying lateral forces of approximately  $\pm 70$  nN on the AFM tip coated with a 50 nm thick gold layer. The contact area of the tip on the mica surface is relatively small compared to that of a bead contact, and the maximum lateral force had to be small enough to be below the static friction at the onset of slip.

In both Figs. 5(a) and 5(b) the data for the forward strokes are plotted only. If plotted the backward strokes overlap the lines of the forward strokes within the noise band, similar to those in Fig. 4(b). Since we are using the data to fit a difference form of (9a),  $\Delta \hat{f} = \alpha_{ij} \Delta \hat{V}^{(l)} + \alpha_{in} \Delta \hat{V}^{(n)}$ , absolute values of the coordinates are not meaningful in these plots. All data sets of both forward and backward strokes were

used to get the least squares fit values of  $\alpha_{ll}$  and  $\alpha_{ln}$  with (20). Errors of  $\alpha_{ll}$  and  $\alpha_{ln}$  are defined by the minimum value of the function  $\Psi$  in (20) divided by the span of  $\hat{V}^{(l)}$  and  $\hat{V}^{(n)}$ , respectively. The lateral force constants of NCC<sup>d</sup> and NCC<sup>d</sup> cantilevers were evaluated with the full least squares fit with (20). However, for other cantilever assemblies only the value of  $\alpha_{ll}$  was evaluated with a single value of  $\hat{V}^{(n)}$  for each cantilever. Then, the least squares fit was made with (20) in which the term of  $\alpha_{ln}$  was neglected for  $\Delta\hat{V}^{(n)}=0$ . The values of  $\alpha_{ll}$  for such tests are average values for forward and backward stroke tests, and the errors are halves of the differences. In Table III, the superscripts 1 and 2 indicate two different cantilevers of the same type. The results for the NC mode cantilevers show that the lateral force constant  $\alpha_{ll}$  of the NCC<sup>d</sup> cantilever with a tip is several times larger than that of a cantilever with a bead. This is because the tip has a height of 3–5  $\mu\text{m}$  and the bead has a height larger than 15  $\mu\text{m}$ . The superscript “d” in Table III indicates the test results for the same cantilever but with slightly different adjustments of the AFM PSPD system. The superscript \* indicates the test results compared with those evaluated by the wedge method in the following subsection.

### C. Comparison with the W-LFC measurement

We performed a side-by-side comparison of our test results with those of W-LFC, the popular wedge calibration method.<sup>4</sup> As mentioned earlier, the wedge method uses frictional slip properties of single asperity contact. In the wedge test the net force normal to the cantilever surface is held fixed, i.e.,  $\hat{V}^{(n)}=\text{constant}$ , while the contact point slides over the surface forwards and backwards on the slopes of the wedge faces. Then the lateral PSPD signal makes a loop. Figure 6(a) shows such a loop made by a silicon tip of a CTB cantilever sliding on a horizontal mica surface. Ever since Mate *et al.* measured nanoscale friction with an AFM (Ref. 2) using a tungsten tip on a graphite surface, such a loop has been analyzed with two major quantities  $\hat{w}$  and  $\hat{\delta}$  related to the frictional slip. Here  $\hat{w}$  represents the width of the loop and  $\hat{\delta}$  the center value of the loop as shown in Fig. 6(a). In the wedge test the two variables  $\hat{w}$  and  $\hat{\delta}$  are measured on the two slopes of the wedge face for different values of  $\hat{V}^{(n)}$ , which are multiplied by  $\alpha_n$  to be converted to those of the normal net force  $\hat{N}$ . Figure 6(b) shows the plots of  $\hat{w}_{\pm}$  and  $\hat{\delta}_{\pm}$  measured on  $\pm$  slopes of the wedge with the CTB\* cantilever-tip assembly listed in Table III. A microfabricated Si slope sample TGG01 from MikroMasch® Inc. was used for the double-slope wedge calibration. The geometry and the dimension of the Si slope sample are shown in the inset of Fig. 6(b). As shown in the figure, it is remarkable that both

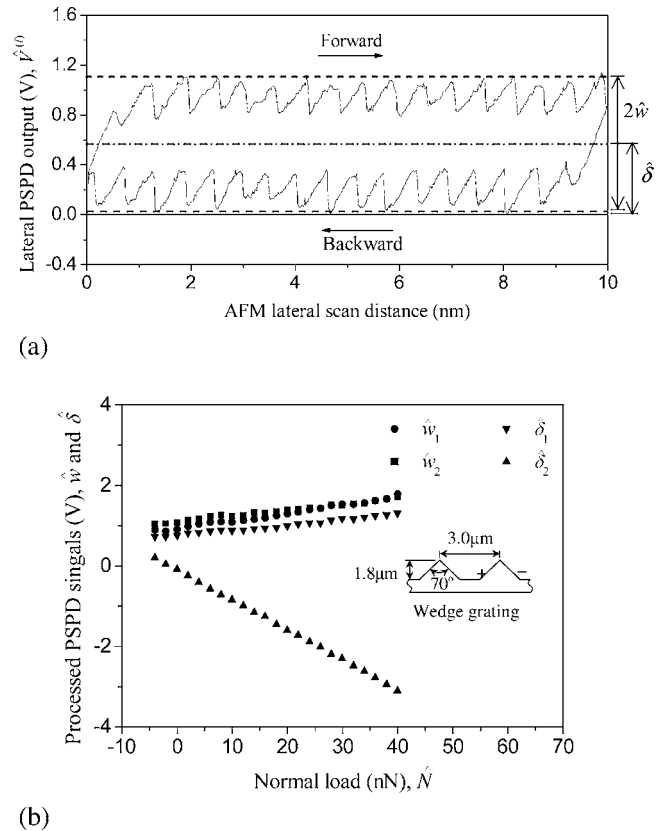


FIG. 6. (a) A friction loop of a contact B tip sliding on a mica surface:  $\hat{w}$  and  $\hat{\delta}$  denote the half-width and the central-value offset of the loop. (b) W-LFC data of  $\hat{w}$  and  $\hat{\delta}$ , which depend on the normal load for the NCC\* tip sliding on the two different slopes of a wedge.

$\hat{w}_{\pm}$  and  $\hat{\delta}_{\pm}$  are linear with respect to  $\hat{N}$ . The constant slopes  $\hat{w}' \equiv d\hat{w}/d\hat{N}$  and  $\hat{\delta}' \equiv d\hat{\delta}/d\hat{N}$  indicate that the differential friction coefficient  $f'$  is also constant within the range of the test. Relationships between friction characteristics of an AFM tip and  $\hat{w}'$  or  $\hat{\delta}'$  are analyzed as per Ogletree *et al.*,<sup>4</sup> but in more detail in Appendix A. The analyses derive the values of  $f'_+$ ,  $f'_-$ ,  $\phi_m$ , and  $\alpha_l$  from the measurement values of  $\hat{w}_{\pm}$  and  $\hat{\delta}_{\pm}$ , provided that the tip radius is negligible, i.e.,  $\xi=0$ . From (6) and (12) we can also get  $\alpha_{ll}=\alpha_l \sec \phi_m$  for  $\xi=0$ .

The calibrated values of  $f'_+$ ,  $f'_-$ ,  $\phi_m$ , and  $\alpha_l$  are summarized in Table IV for two different cantilever assemblies, NCC\* and CTB\*. The cantilever-tip assemblies used for this comparison are the ultralever contact B tip (CTB\*-tip with nominal spring constant of 0.4 N/m) and noncontact C tip coated with a 50 nm thick gold layer (NCC\*-tip with nominal spring constant of 13 N/m) from Veeco Inc. Since the wedge method gives  $\alpha_{ll}$  only in terms of the normal force

TABLE IV. Force constants  $\alpha_{ll}$  measured by W-LFC for the CTB\*-tip and NCC\*-tip assemblies.

Cantilever	$\hat{w}'_+$ (V/nN)	$\hat{w}'_-$ (V/nN)	$\hat{\delta}'_+$ (V/nN)	$\hat{\delta}'_-$ (V/nN)	$f'_+$	$f'_-$	$\phi_m$ (°)	$\alpha_{ll}$ (nN/V)
NCC*	0.001 66	0.001 69	0.001 92	-0.005 27	0.2289	0.2322	38.0	689.80
CTB*	0.019 73	0.014 35	0.013 02	-0.074 56	0.2148	0.1631	49.6	36.533

constant of the cantilever, we had to measure or estimate the normal force constant additionally. The same cantilever-tip assemblies were also calibrated using our calibrator and the results are shown in Table III. The stiff cantilever-tip assembly NCC\* was calibrated on the stiffest magnetic spring system of PG-2, and the compliant cantilever-tip assembly CTB\* was calibrated on the most compliant magnetic spring system of PG-6.

It is observed that  $f'_+$  and  $f'_-$  are practically the same for the contacts between the gold coating and the silicon surface, while they are distinctly different for the contacts between the silicon tip and the silicon surface. This dissimilarity is believed to be caused by different frictional properties of different crystallographic surfaces of silicon for the nonsymmetric contact friction made by nonvanishing  $\phi_m$ . It is also remarkable that the nominal misfit angles of the AFM tips,  $\phi_m$ , are very large,  $38^\circ$  for NCC\* and  $50^\circ$  for CTB\*. Here the nominal misfit angle  $\phi_m$  denotes the significance of the crosstalk effect, which comes from both mechanical and optical misalignments. We measured the ratios  $\Delta\hat{V}^{(l)}/\Delta\hat{V}^{(n)}$  as 0.03 for a cantilever vibrating in air predominantly in a bending mode and 0.15 for a cantilever under normal contact with a substrate surface. These results indicate that the crosstalk effect came mostly from the shear center misalignment for the NCC\* cantilever. While it is crucial for the W-LFC calibration whether the crosstalk comes from the mechanical or the optical misalignment, it does not matter for the D-LFC calibration. This is a strong advantage of using D-LFC, over W-LFC, in addition to many other reasons such as better accuracy and simplicity.

Since the W-LFC requires the normal force constant to evaluate the lateral force constant  $\alpha_{ll}$ , at first we used the vendor's nominal normal spring constants for CTB\* and NCC\* cantilevers. Then, the lateral force constant of CTB\* turned out to be 36.53 nN/V and it is about 26% smaller than the D-LFC value of 49.61 nN/V. The W-LFC also gave the lateral constant of NCC\* as 469.25 nN/V, which is approximately 21% lower than the D-LFC value of 591.92 nN/V. As we noticed that the vendor's nominal normal spring constant can be a major error source for the estimation of the lateral force constant, we calibrated the normal spring constant and the PSPD angle sensitivity constant of the triangular cantilever NCC\* independently. In this calibration we employed the method of Sader *et al.*,<sup>18</sup> deflecting the cantilever against another rectangular cantilever of known stiffness<sup>19</sup> and against a hard surface. Even if we carried out this calibration, the lateral force constant  $\alpha_{ll}$  of NCC\* measured by the wedge method turned out to be 689.80 nN/V, which is about 16.5% larger than the value measured by D-LFC. The discrepancies between the W-LFC and D-LFC values are believed to be coming mainly from two additional sources of errors in the wedge method. One is from the assumption of  $\xi=0$  employed in the wedge method and the other from uncertainties of reading  $\hat{w}'$  and  $\hat{\delta}'$  off the friction loop as described in Sec. II.

#### IV. DISCUSSIONS

As described in the previous sections, a direct calibration apparatus, "diamagnetic lateral force calibrator (D-LFC),"

has been developed in this article to calibrate the full set of the AFM lateral force constants with high accuracy. It is designed to have an accuracy of calibration better than 0.1%. Some possible operational error sources were also investigated. One such source is the reciprocation rate effect of the spring displacement in the diamagnetic levitation system during the calibration process. It is noticed that the viscous drag effect hardly plays a role in the calibration process as shown in Table II. As a rough estimation, the typical value of  $c_{11}$  is  $\sim 10 \mu\text{N s/m}$ , the magnetic spring constant  $k_{11}$  has a typical value of 10 pN/nm, and the spring displacement is  $\sim 20 \mu\text{m}$  at 0.5 Hz during the calibration. Then, the magnetic spring exerts a force of  $\sim 200 \text{ nN}$  while the maximum total viscous drag force is  $\sim 0.2 \text{ nN}$ , which is about 0.1% of the magnetic spring force. Moreover, during the calibration process the graphite is stuck to the tip so that the air drag force will be further reduced. Hence, in most cases, the viscous drag effect is negligible. It was confirmed by experiments that the calibrated force constants hardly depend on the reciprocation rate of the  $20 \mu\text{m}$  spring displacement from 0.25 to 4 Hz. In addition, dependence of the calibration on the contact location of the AFM tip on the levitated PG-mica composite sheet was tested as another possible operational error source. Experiments show that, within a radial distance of 1 mm from the center of the levitated PG-2 sheet, variation of the measured lateral force constant was less than 0.5%. Furthermore, experiments confirmed that the lateral magnetic spring constant of the systems which we have tested is insensitive to the normal load within the range that a microfabricated cantilever can achieve, i.e., up to a few micronewtons. All these experiments prove that D-LFC is a very reliable and robust method of calibration, which is relatively easy to implement.

We summarize our conclusions as follows: (A) Deformation characteristics of AFM cantilever-tip and -bead assemblies have been analyzed for general radii of curvature of the tips in frictional contact. The analysis has clarified various difficulties in calibrating AFM lateral force constants, encountered in indirect and semidirect methods of calibration. It has been found that the major difficulties come from the location uncertainty of the shear center of the cantilever. The analysis also has characterized the wedge method completely. (B) This analysis has introduced new AFM response variables: the normal force constant  $\alpha_n$ , the lateral force constant  $\alpha_{ll}$ , the crosstalk lateral force constant  $\alpha_{lm}$ , and the generic lateral force constant  $\alpha_l$ . Once  $\alpha_{ll}$ ,  $\alpha_{lm}$ ,  $\alpha_n$ , and  $\alpha_l$  are measured, the intrinsic structural variables  $\phi_m$  and  $\xi$  can be evaluated from (10). The analysis led to the development of a direct method of AFM lateral force constants calibration, D-LFC for AFM systems. (C) A magnetic-spring load cell system was built by levitating a pyrolytic graphite sheet with four NdFeB magnets. The system comprises the D-LFC for an AFM system. Measurement of the levitated mass and the free vibration natural frequency provided a spring constant for the system on the order of 10 pN/nm. The spring constant was measured with  $10^{-4}$  accuracy and was used for calibrating the AFM lateral constants ranging from a few tens of nN/V to several hundreds of nN/V. (D) The calibration data exhibit remarkable linearity of the lateral PSPD

output of the AFM, with respect to both lateral and normal loads, as shown in Fig. 5. Because of the linearity, a simple least squares fit data processing provides both the lateral force and the cross talk lateral force constants with an accuracy on the order of 0.1% for AFM cantilever-tip and -bead assemblies. Implementation of the calibration procedure and the data processing was found to be robust and relatively easy. (E) The lateral force constants,  $\alpha_{ll}$ , of two different AFM cantilever-tip systems were measured with the D-LFC and compared with the values estimated by the W-LFC. Analyses indicate that the wedge method is only applicable to a sharp tip, if the shear center misalignment of the cantilever is properly treated, and the comparison shows that even for sharp tips the wedge method estimated the value of  $\alpha_{ll}$  with errors more than 15% for two different cantilevers. In contrast, the D-LFC could measure not only the  $\alpha_{ll}$  but also the crosstalk lateral force constant  $\alpha_{ln}$  with better than 0.5% accuracy without a complex interpretation of all those intrinsic quantities. (F) The new D-LFC capability for calibrating simultaneously both  $\alpha_{ll}$  and  $\alpha_{ln}$  has made it possible to measure the absolute lateral forces experienced in nano- and microfriction experiments as well as in molecular and cellular biomechanical testings. In particular, the capability of calibrating AFM cantilever-bead assemblies with large tip radii will provide new opportunities in molecular and cellular biomechanical testings. It is also noticed that because of its *in situ* feature, the real sample can be immediately tested without interruption and readjustment of the laser beam, which can improve the accuracy of the measurement for most foreseeable experiments.

## ACKNOWLEDGMENTS

The authors gratefully acknowledge valuable discussions with Dr. Jun Lou of Rice University. This work is supported in part by the Nano and Bio Mechanics Program, under award CMS-0511961, and in part by the MRSEC Program, under award DMR-0520651, of the National Science Foundation.

## APPENDIX A: ANALYSIS OF AFM RESPONSES FOR A W-LFC MEASUREMENT

Since W-LFC uses the slope information, i.e., the differential friction coefficient, of the friction law, it is convenient to use the difference of (5) as

$$\Delta N_\eta (1 - \xi) \sin(\phi^* - \phi_m) + \text{sgn}(\eta) \Delta f_\eta \{ (1 - \xi) \cos(\phi^* - \phi_m) + \xi \} = \alpha_l \Delta \hat{V}_\eta, \quad \eta = a \text{ or } b, \quad (\text{A1})$$

where  $\text{sgn}(\eta) = 1$  for  $\eta = a$  and  $-1$  for  $\eta = b$ . Dividing (A1) with  $\Delta N_\eta$  and assuming that  $f'_\eta = \Delta f_\eta / \Delta N_\eta$  is fairly constant, respectively, with respect to the variation of  $N_\eta$  within the range of the calibration test, (A1) can be reduced to

$$\frac{(1 - \xi) \sin(\phi^* - \phi_m) + \text{sgn}(\eta) f'_\beta \{ (1 - \xi) \cos(\phi^* - \phi_m) + \xi \}}{\cos \phi^* - \text{sgn}(\eta) f'_\eta \sin \phi^*} = \alpha_l \hat{V}'_\eta, \quad (\text{A2})$$

where  $\hat{V}'_\eta = \Delta \hat{V}_\eta / \Delta \hat{N}_\eta$  and  $\Delta \hat{N}_\eta / \Delta N_\eta = \cos \phi^*$

$-\text{sgn}(\eta) f'_\eta \sin \phi^*$  was employed from the geometry in Fig. 1. Subtracting (A2) of  $\eta = b$  from (A2) of  $\eta = a$ , and introducing  $D = (1 - \xi) \cos \phi_m + \xi \cos \phi^*$ , we get

$$\frac{(f'_a + f'_b) D}{2(\cos \phi^* - f'_a \sin \phi^*)(\cos \phi^* + f'_b \sin \phi^*)} = \alpha_l \hat{w}'. \quad (\text{A3})$$

If we add (A2) of  $\eta = a$  and (A2) of  $\eta = b$ , it can be reduced to

$$\frac{-(1 - \xi) \sin \phi_m + \sin \phi^* \{ (1 - \xi)(1 + f'_a f'_b) \cos(\phi^* - \phi_m) + \xi f'_a f'_b \} + (D/2)(f'_a - f'_b)}{(\cos \phi^* - f'_a \sin \phi^*)(\cos \phi^* + f'_b \sin \phi^*)} = \alpha_l \hat{\delta}'. \quad (\text{A4})$$

Here,  $\hat{w}$  indicates the width of the friction loop and  $\hat{\delta}$  the offset of the loop center as shown in Fig. 6(a). Ogletree *et al.*<sup>4</sup> used an assumption that  $\xi = 0$  to get the value of  $\alpha_{ll} = \alpha_l / \cos \phi_m$ . It is noticed in (A3) that  $\hat{w}'_+ = \hat{w}'_-$  for symmetric wedges, i.e.,  $\phi^* = \pm \phi_w$ , with a wedge angle value of  $\phi_w$ . It is also noticed that the quantity  $\hat{\delta}'_+ - \hat{\delta}'_-$  derived from (A4) does not depend on  $\phi_m$  for symmetric wedges, but only if  $\xi = 0$ . Therefore, they could evaluate  $\alpha_{ll}$  for  $\xi = 0$  without evaluating  $\alpha_l$  and  $\phi_m$  explicitly. However, the method cannot be applied to cases of non-negligible tip radius, i.e.,  $\xi \neq 0$ .

## APPENDIX B: DYNAMIC CHARACTERISTICS OF THE LEVITATED MASS IN A D-LFC

The Lagrangian of the magnetic spring system of the D-LFC is given by

$$L = \frac{1}{2} \sum_{i,j=1}^3 [m^{(L)} \delta_{ij} \dot{x}_i^{(0)} \dot{x}_j^{(0)} + I_{ij}^{(L)} \dot{\Omega}_i \dot{\Omega}_j - k_{ij}^{(m)} x_i^{(0)} x_j^{(0)} - \kappa_{ij}^{(m)} \Omega_i \Omega_j] - m^{(L)} g x_3^{(0)}, \quad (\text{B1})$$

where  $\delta_{ij}$  is the Kronecker delta and  $I_{ij}^{(L)}$  the moment of inertia of the levitating mass, and the dot on top of a variable indicates the time derivative of the variable. Then, the Euler equation becomes

$$m^{(L)} \ddot{x}_i^{(0)} + \sum_{j=1}^3 k_{ij}^{(m)} x_j^{(0)} = - \sum_{j=1}^3 c_{ij} \dot{x}_j^{(0)}, \quad (\text{B2a})$$

$$\sum_{j=1}^3 [I_{ij}^{(L)} \ddot{\Omega}_j + \kappa_{ij}^{(m)} \Omega_j] = - \sum_{j=1}^3 d_{ij} \dot{\Omega}_j, \quad (\text{B2b})$$

for which we assumed that the viscous drag of the air and the eddy current is linearly proportional to the velocity of the motion. The drag is represented by  $c_{ij}$  for translational motion and by  $d_{ij}$  for rotational motion. Then, the vibration characteristic equation of (17) turns out to be

$$\det[m^{(L)} \omega^2 \delta_{ij} + \omega c_{ij} + k_{ij}^{(m)}] = 0, \quad (\text{B3a})$$

$$\det[\omega^2 I_{ij}^{(L)} + \omega d_{ij} + \kappa_{ij}^{(m)}] = 0. \quad (\text{B3b})$$

Therefore, we can have six complex conjugate pairs of  $\omega$ , corresponding to the six dynamic eigenfrequencies of the magnetic levitation spring system for underdamped oscillations. Since we are interested only in a principal vibration in the  $x_1$  direction, (B2) is reduced to (16) in Sec. II B.

- <sup>1</sup>G. Binnig, C. F. Quate, and C. Berber, *Phys. Rev. Lett.* **56**, 930 (1986).
- <sup>2</sup>C. M. Mate, G. M. McClelland, R. Erlandsson, and S. Chiang, *Phys. Rev. Lett.* **59**, 1942 (1987).
- <sup>3</sup>R. W. Carpick, N. Agrait, D. F. Ogletree, and M. Salmeron, *Langmuir* **12**, 3334 (1996).
- <sup>4</sup>D. F. Ogletree, R. W. Carpick, and M. Salmeron, *Rev. Sci. Instrum.* **67**, 3298 (1996).
- <sup>5</sup>H. J. Butt, *J. Colloid Interface Sci.* **166**, 109 (1994).
- <sup>6</sup>M. Kappl and H. J. Butt, *Part. Part. Syst. Charact.* **19**, 129 (2002).
- <sup>7</sup>M. Varenberg, I. Etsion, and G. Halperin, *Rev. Sci. Instrum.* **74**, 3362 (2003).
- <sup>8</sup>C. T. Gibson, G. S. Wastson, and S. Myhra, *Wear* **213**, 72 (1997).
- <sup>9</sup>E. Liu, B. Blanpain, and J. P. Celis, *Wear* **192**, 141 (1996).
- <sup>10</sup>R. J. Warmack, X. Y. Zheng, T. Thundat, and D. P. Allison, *Rev. Sci. Instrum.* **65**, 394 (1994).
- <sup>11</sup>J. M. Neumeister and W. A. Ducker, *Rev. Sci. Instrum.* **65**, 2527 (1994).
- <sup>12</sup>R. G. Cain, S. Biggs, and N. W. Page, *J. Colloid Interface Sci.* **227**, 55 (2000).
- <sup>13</sup>G. Bogdanovic, A. Meurk, and M. W. Rutland, *Colloids Surf., B* **19**, 397 (2000).
- <sup>14</sup>S. Jeon, Y. Braiman, and T. Thundat, *Appl. Phys. Lett.* **84**, 1795 (2004).
- <sup>15</sup>R. G. Cain, M. G. Reitsma, S. Biggs, and N. W. Page, *Rev. Sci. Instrum.* **72**, 3304 (2001).
- <sup>16</sup>J. D. Holbery, V. L. Eden, M. Sarikaya, and R. M. Fisher, *Rev. Sci. Instrum.* **71**, 3769 (2000).
- <sup>17</sup>M. D. Simon and A. K. Geim, *J. Appl. Phys.* **87**, 6200 (2000).
- <sup>18</sup>J. E. Sader, J. W. M. Chon, and P. Mulvaney, *Rev. Sci. Instrum.* **70**, 3967 (1999).
- <sup>19</sup>Veeco Metrology, Santa Barbara, CA.